Ultrafast x-ray detection of low-spin iron in molten silicate under deep planetary interior conditions

Sang-Heon Shim, Byeongkwan Ko, Dimosthenis Sokaras, Bob Nagler, He Ja Lee, Eric Galtier, Siegfried Glenzer, Eduardo Granados, Tommaso Vinci, Guillaume Fiquet, et al.

GEOPHYSICS

Ultrafast x-ray detection of low-spin iron in molten silicate under deep planetary interior conditions

Sang-Heon Shim[1]*, Byeongkwan Ko[1]†, Dimosthenis Sokaras[2], Bob Nagler[2], He Ja Lee[2], Eric Galtier[2], Siegfried Glenzer[2], Eduardo Granados[2]‡, Tommaso Vinci[3], Guillaume Fiquet[4], Jonathan Dolinschi[1]§, Jackie Tappan[1], Britany Kulka[1]||, Wendy L. Mao[2,5]*, Guillaume Morard[4,6]*, Alessandra Ravasio[3]*, Arianna Gleason[2,5]*, Roberto Alonso-Mori[2]*

The spin state of Fe can alter the key physical properties of silicate melts, affecting the early differentiation and the dynamic stability of the melts in the deep rocky planets. The low-spin state of Fe can increase the affinity of Fe for the melt over the solid phases and the electrical conductivity of melt at high pressures. However, the spin state of Fe has never been measured in dense silicate melts due to experimental challenges. We report detection of dominantly low-spin Fe in dynamically compressed olivine melt at 150 to 256 gigapascals and 3000 to 6000 kelvin using laser-driven shock wave compression combined with femtosecond x-ray diffraction and x-ray emission spectroscopy using an x-ray free electron laser. The observation of dominantly low-spin Fe supports gravitationally stable melt in the deep mantle and generation of a dynamo from the silicate melt portion of rocky planets.

INTRODUCTION

Early Earth was likely subject to highly energetic impacts. The heat energy released from the impacts was likely sufficient to induce global melting events and sustained a silicate magma ocean hundreds of kilometers deep (*1*). Molten silicates and Fe alloys in the magma ocean were then separated by their density difference, leading to the formation of the Fe-rich core. Crystallization of the magma ocean may have begun soon after the Moon-forming giant impact event and may have formed large-scale chemical structures in the mantle some of which may have survived up to now (*2*, *3*). Such primordial structures may be responsible for the geochemical signatures measured in ocean island basalts and some of the seismic structures found in the deep mantle, such as large-low shear velocity provinces and ultralow velocity zones (*4*). Their chemical composition and spatial extension are intrinsically controlled by magma ocean properties and dynamics (*5*, *6*).

One of the key parameters for modeling magma ocean dynamics is the density contrast between coexisting solid and molten silicates (*5*). At low pressures (or shallow depths), silicate melts have a larger molar volume compared to solid silicates of similar composition. Because of the higher compressibility of silicate melts, the volume difference between solid and molten silicates becomes smaller at higher pressure (*7*). However, theoretical studies indicate that the higher compressibility of a melt with mantle-relevant composition cannot alone induce density crossover such that the melt becomes denser than the solid within the mantle (*8*). Instead, the density contrast is mainly controlled by the Fe partitioning between solid and molten silicates under the pressure-temperature conditions expected for the deep magma ocean. An earlier experiment reported a sharp transition from high-spin (HS) to low-spin (LS) Fe at 70 GPa in cold-compressed silicate glass (*9*). The similarity between the pressure where the spin transition of Fe in silicate glass is observed, and the pressure where Fe partitions strongly into the partial melt of pyrolite over coexisting bridgmanite (*9*, *10*) suggests a possible link between these two processes (*9*), because a smaller ionic size of LS Fe compared to HS Fe can result in more compact packing of atoms and as a result of an energetically more favorable state at high pressures (*11*). Therefore, if silicate melt can accommodate more LS Fe compared to the solid, Fe may preferentially partition into the liquid phase. Recent ab initio calculations for (Mg, Fe)O indeed support the link between the partitioning behavior and the spin state of Fe (*12*). In addition, the spin behavior is essential for modeling the physical properties of Fe-bearing silicate melts, such as elastic properties and electrical conductivity (*13*).

More recent experiments on cold-compressed glasses with similar compositions, however, have reported a much more gradual transition from HS to LS Fe (*14*, *15*). Furthermore, unlike the earlier study (*9*), the recent studies have shown that a substantial fraction of Fe remains HS (35 to 100%) in silicate glasses even at the pressures expected for the core-mantle boundary (CMB). It is important to note that using cold-compressed glasses as analogs for melts has important potential limitations. While the long-range structural behavior between glasses and melts may be similar (*16*), it is important to note that the spin state of Fe is mainly controlled by the interaction with nearby oxygen ligands, and therefore, the local environment is key for the transition (*17*). In the case of cold compression at 300 K, the glass structure may not be fully

[1]School of Earth and Space Exploration, Arizona State University, Tempe, AZ 85287, USA. [2]SLAC National Accelerator Laboratory, 2575 Sand Hill Rd., Menlo Park, CA 94025, USA. [3]Laboratoire pour l'Utilisation des Lasers Intenses (LULI), Ecole Polytechnique, CNRS, CEA, UPMC, 91128 Palaiseau, France. [4]Sorbonne Université, Institut de Minéralogie, de Physique des Matériaux et de Cosmochimie, IMPMC, Museum National d'Histoire Naturelle, UMR CNRS 7590, 4 Place Jussieu, 75005 Paris, France. [5]Department of Earth and Planetary Sciences, Stanford University, Stanford CA 94305, USA. [6]Université Grenoble Alpes, Universé Savoie Mont Blanc, CNRS, IRD, Université Gustave Eiffel, ISTerre, 38000 Grenoble, France.
*Corresponding author. Email: sshim5@asu.edu (S.H.-S.); wmao@stanford.edu (W.M.); guillaume.morard@univ-grenoble-alpes.fr (G.M.); alessandra.ravasio@polytechnique.edu (A.R.); ariannag@stanford.edu (A.G.); robertoa@slac.stanford.edu (R.A.-M)
†Present address: Michigan State University, East Lansing, MI 48823, USA.
‡Present address: CERN, 1211 Geneva 23, Switzerland.
§Present address: Universität Bayreuth, Universitätsstraße 30, 95447 Bayreuth, Germany.
||Present address: Oxford University, Wellington Square, Oxford OX1 2JD, UK.

relaxed, and therefore, the local environments may be different from those expected for melts, especially at higher pressures. Therefore, it is important to conduct direct measurements for silicate melts at high pressures.

Ab initio calculations (*5*, *12*, *18*) have found that the population of LS Fe in melts increases continuously over a large pressure range and becomes dominant at the pressure conditions of the Earth's CMB, which is different from the experimental observations for cold-compressed glass (*9*, *14*, *15*). However, theoretical simulations on the Fe spin state in melts are challenging under extreme conditions due to the diverse coordination environments expected in melt structures and the large thermal effects. Modeling spin ordering of Fe in oxides is expensive and requires different approximations on the exchange-correlation evolution in pressure and temperature (*19*). Therefore, the spin state of Fe in silicate melt at high pressure-temperature remains uncertain (*20*, *21*).

Despite the importance of determining Fe spin state in silicate melts at high pressures, direct experimental measurements have been extremely challenging. In static compression experiments, the silicate sample needs to be sustained in a molten state at the simultaneous high pressure and temperature conditions existing deep in the mantle for a sufficiently long time to collect the weak Fe $K\beta_{1,3}$ emission spectra from the ~10^{-11}- to 10^{-11}-cm^3 sample volume. Laser heating can raise the temperature of silicate samples above melting, but the heating is localized to a small portion of the sample and can introduce severe chemical inhomogeneity (particularly in the case of Fe) along thermal gradients if the high temperature needs to be maintained for more than a few seconds (*22*). Even at the third-generation synchrotron facilities, the collection of an Fe $K\beta_{1,3}$ emission spectrum under these conditions can require several hours for the low Fe systems relevant for the mantles of rocky planets.

Here, we report the direct experimental measurements of the spin state of Fe in a silicate melt of San Carlos olivine composition at pressures more than 150 GPa and temperatures more than 3000 K obtained by combining laser-driven shock compression and ultrafast x-ray diffraction (XRD) and emission spectroscopy (XES) from an x-ray free electron laser (XFEL) (*23*). The starting material was olivine from San Carlos, Arizona, with a measured composition of $(Mg_{0.88}Fe_{0.12})_2SiO_4$ (see Materials and Methods and table S1). Experiments were performed at the Matter in Extreme Conditions (MEC) end-station of the Linac Coherent Light Source, SLAC (Stanford Linear Accelerator Center) National Accelerator Laboratory. High pressure and temperature conditions in the olivine samples were obtained using laser-driven dynamic compression. We used the MEC long pulse ($\tau \simeq 10$ ns) high-energy (E_L up to 60 J at λ_L = 527 nm) laser beam focused (~150-μm smoothed focal spot) on the target to reach intensities of a few 10^{13} W/cm ^{2} and generate a compression shock wave. Optical velocity interferometers were used to monitor shock propagation and infer the thermodynamic state of the compressed sample (fig. S1). A ~50-fs single x-ray pulse from the XFEL (50-μm spot diameter) was used to probe the compressed sample. XRD and XES were simultaneously collected; see schematic illustration of the experimental setup that is presented in Fig. 1.

RESULTS

Our XRD patterns of shocked olivine show similar features to those found in previous works on diverse shock-compressed silicates (*16*, *24*, *25*). As in those previous studies, at low pressures (up to ~60 GPa), we observed crystalline structures from compressed olivine and its high-pressure polymorphs. As pressure increases, the appearance of two broad scattering contributions around 27 and 35 nm^{-1} (Q_1 and Q_2 in Fig. 2, A and B) reveals the amorphization of the crystalline sample before melting, similar to the observations for enstatite and forsterite (*24*, *25*). With increasing compression, these peaks shift to higher diffraction angles (or higher momentum transfer, Q in nm^{-1}) and Q_2 gains intensity, eventually becoming more intense than Q_1. Cold compression studies of silicate glasses (*16*, *26*) showed that the high-pressure behaviors of Q_1 and Q_2 are related to a structural change from four- to sixfold coordinated Si. Moreover, recent work (*16*) reported the same Q_1-Q_2 trends with density for cold-compressed silicate glasses and shock-compressed silicate glasses and melts, suggesting that the major pressure-induced transformations are very similar between these two systems. The Q_1 and Q_2 positions of our olivine shots compared to forsterite (*25*) or $MgSiO_3$ glass (*24*) as a function of compression rate (ρ/ρ_0, where ρ and ρ_0 are densities at high pressures and at 1 bar, respectively) show similar trends, considering both thermal effects and different initial densities (see Materials and Methods and fig. S2). The disordered olivine structure measured here under shock compression follows the same, universal Q_1-Q_2 trend as a range of different Mg-bearing amorphous and liquid silicates (fig. S3). The remarkable agreement between our data and both statically and dynamically compressed silicates found in literature is consistent with the assumption that the intermediate range structures of glasses and melts behave similarly with pressure (*26*).

Pressures for the majority of our olivine data estimated from optical measurements (see Materials and Methods for more details) lie above the intersection of the olivine Hugoniot with its melting curve, around 150 GPa (Fig. 3) (*27*). In the pressure range corresponding to liquid state studied here (150 to 256 GPa), we estimated a temperature range between 4000 and 6000 K following the previous studies performed using a combination of multiple techniques (fig. S5) (*27*, *28*).

The XES measured simultaneously with XRD during dynamic compression shows a systematic shift of the $K\beta_{1,3}$ peak to a lower energy and a decrease in the intensity of the satellite peak at 7045 eV ($K\beta'$). Even when the signal-to-noise ratios are relatively low (Fig. 2, D and E), the strong red shift of the main line identifies the transition to LS unambiguously. This finding is clear evidence of an increase in the Fe LS population with increasing pressure along the Hugoniot (Fig. 2) (*17*).

The XES data are processed using the integrated absolute difference (IAD) method (*29*). The shift of the main peak indicates a large decrease in the spin moment in the pressure range (Fig. 2). A spectrum processed with the integrated relative difference (IRD) method (*15*) reveals a near absence of satellite peak intensity at the pressures above the intersection between the melting curve and olivine Hugoniot (see fig. S4). Regardless of the XES processing method (IAD or IRD), data support almost complete transition to LS Fe for olivine melt at pressures above 150 to 256 GPa, which is the peak pressure of this study. For the conversion of the data to a total spin momentum, it is necessary to know the spectrum for LS Fe in

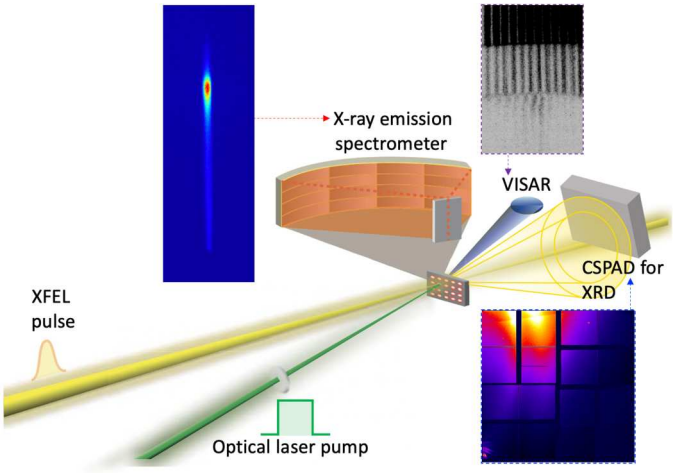

Fig. 1. Schematic diagram of the experimental setup showing the pulsed x-ray beam from the XFEL probing the sample targets during the laser-generated shock compression. The x-ray (yellow) arrival time was adjusted relative to the optical laser pump (green) to probe the sample at peak compression. Three diagnostics/techniques were used concomitantly for each single x-ray pulse: The Fe *K*β XES spectrum was collected using a dispersive multicrystal XES emission spectrometer (*45*) to extract information about the spin state of Fe (top left inset), the XRD pattern in the forward scattering direction provides structural information (bottom right inset), and the velocity interferometer system for any reflector (VISAR) data were also collected to obtain the shocked sample thermodynamic state (top right inset).

olivine melt, which is unknown. If we consider the LS IAD values from the pyroxene glass dataset (*14*), then we can estimate that more than 70% of Fe should be LS for olivine melt at pressures above 150 GPa (Fig. 3).

DISCUSSION

By combining an extremely bright femtosecond XFEL beam with dynamic compression, we have successfully measured the spin state of Fe in olivine melt at deep mantle pressures and temperatures. Simultaneously, we measured XRD of the shocked olivine melt, providing an unprecedented view on the atomic-scale structure of silicate melt: from the few angstrom scale of next neighbor interactions between atoms from XES to the few hundred-nanometer scale structural information from XRD. The XES measurement provides the first direct experimental evidence for predominant LS Fe in a dense silicate melt and demonstrates the importance of in situ measurements at both high pressure and high temperature. While the simultaneously measured XRD indicates the long-range ordering of the silicate melt remains similar to cold-compressed glasses, XES reveals a very different picture: Structural relaxation at the short-range level enables conversion of the spin state of Fe to a LS configuration at high pressure and high temperature in silicate melt, which is not the case for cold-compressed glasses. First-principles studies have suggested 80 to 90% of Fe in LS at 4000 K and 140 GPa for pyroxene melt (*8*) and a complete transition to LS at 140 GPa and 4000 K for pyrolitic melt (*5*). Therefore, our results on olivine melt with predominantly LS Fe at 150 GPa are in general agreement with these theoretical predictions, providing direct experimental confirmation of the results from first-principles calculations.

The existence of a predominantly LS state of Fe in silicate melts demonstrated in this study has important implications for rocky planets (Fig. 4). Compilation of existing data on pyrolitic compositions shows that Fe partitioning to liquid increases between 20 and 100 GPa and then becomes nearly constant at pressures above 120 GPa (*20*). This observation is compatible with our observation of nearly complete LS state for Fe in silicate liquids at pressures between 150 and 256 GPa. In (Mg,Fe)O, an ab initio study (*12*) found that while more Fe partitions into the oxide melt over the entire pressure range expected for the Earth's mantle, the HS-to-LS transition in the solid phase reduces the amount of Fe partitioned into the oxide melt. The result strongly indicates that Fe preferentially partitions into the phase, which can offer a local structure more favorable for LS Fe. Therefore, the dominant LS spin state of Fe in silicate melt shown in this study at the pressures above 150 GPa will lead to enhance Fe partitioning into silicate melt.

Although the exact value for the Fe partition coefficient is under debate (*10*, *30*, *31*), all the existing data indicate that Fe preferentially partitions into silicate melt over solid. Furthermore, even when the weakest Fe partitioning to melt value (*31*) is used, the density of the silicate melt still remains higher than coexisting solids in a crystallizing magma ocean (*5*). Therefore, combined with these results, our measurements of predominant LS Fe in liquid silicates at pressures above 150 GPa support gravitationally stable silicate melt in the deep interiors of Earth-size and larger rocky planets.

Some models have suggested that an early magma ocean may have suppressed dynamo generation from the Earth's core but also generated one within itself, because of elevated electrical conductivity promoted by Fe in the silicate melt (*6*, *32*). A recent density functional theory study showed that Fe being LS would further increase electrical conductivity, assisting dynamo generation in a basal magma ocean in early Earth (*13*). The presence of highly conductive molten silicates at the base of the mantle may also have important implications for other rocky planets. For example, a recent model proposed that a basal magma ocean might have existed in Venus for a much longer period than Earth because of the higher internal temperatures expected for Venus (*33*). The model hypothesized that a dynamo could be generated solely from a Venusian basal magma ocean.

Much larger versions than our solar system rocky planets exist, super-Earths, most of which lie within 1 to 1.6 Earth radius, $R(E)$, in the current exoplanet database (Fig. 4). For a ~1.2 $R(E)$ planet with Earth-like core mass fraction and composition, the pressure at the CMB is expected to reach ~280 GPa, which is the maximum pressure achieved in our experiments (see Materials and Methods). Assuming that LS Fe begins to be the dominant component above 75 to 100 GPa [pressure inferred from the Fe partitioning behavior change found in silicate melt (*9*, *10*, *20*)], a ~1.2 $R(E)$ super-Earth could have LS Fe present in the bottom 60% of its silicate magma ocean. Therefore, LS Fe could also be the prevailing electronic configuration of Fe in the deep interiors of super-Earths up to 1.2 $R(E)$. The magma oceans of the many super-Earths may have a diverse range of Mg/Si ratios, FeO content, and heat producing element concentration, which could affect the LS Fe magma in Fig. 4. However, the main purpose of Fig. 4 is to demonstrate the effects of size (or internal pressure) on the spin state of Fe in silicate melt.

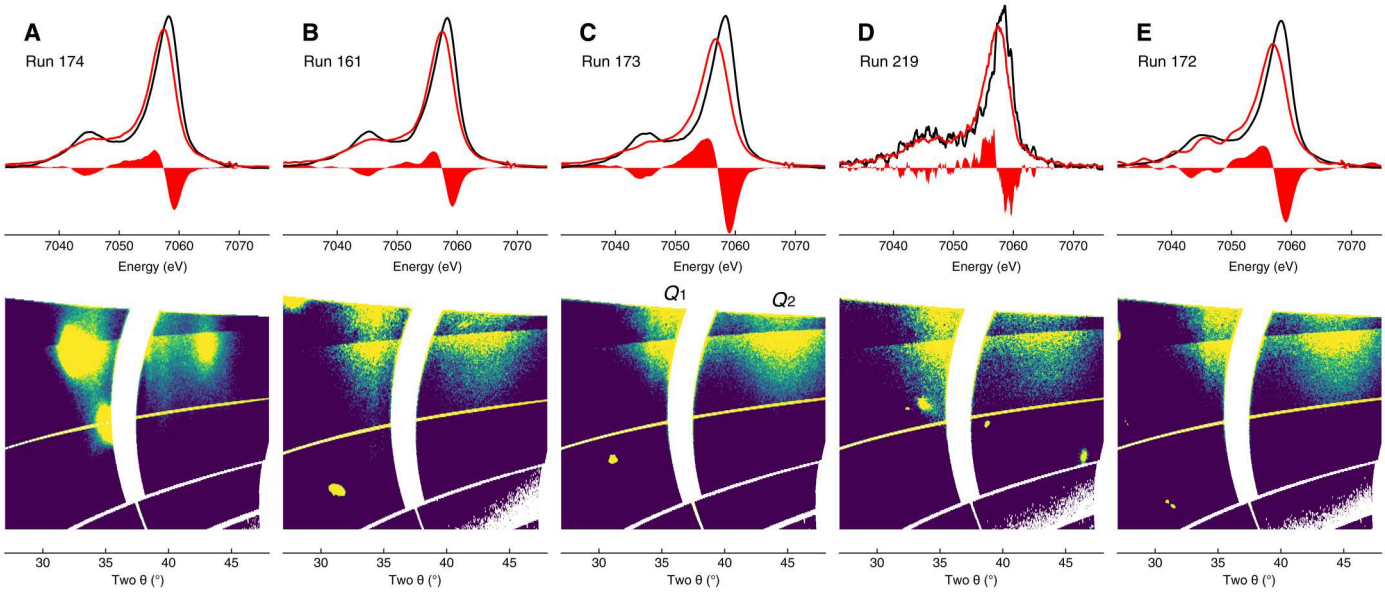

Fig. 2. X-ray emission spectra and XRD images for San Carlos olivine under shock compression. (**A**) 86 GPa, (**B**) 173 GPa, (**C**) 203 GPa, (**D**) 203 GPa, and (**E**) 256 GPa (see run table in table S1). The Fe *K*β XES signal was measured before (black) and during (red) the laser-induced shock. Differences between these two spectra are shown in solid red. A decrease in spin moment results in larger differences (an intense decrease in the low-energy satellite peak and a position shift of the main peak to lower energy). The two broad peaks in the XRD patterns (Q_1 and Q_2) are from the amorphized samples. The gap in the image is from the spacing between CSPADs (Cornell-SLAC Pixel Array Detectors), and the bright spots are from LiF single crystals.

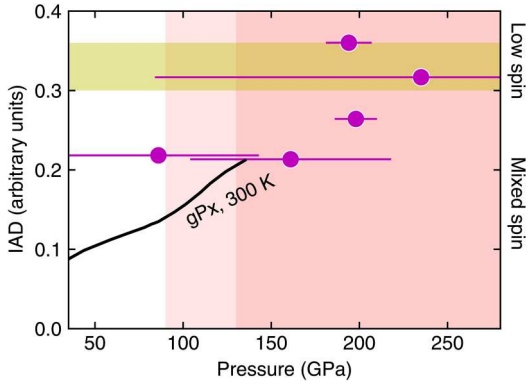

Fig. 3. Estimated spin moment for shocked olivine melt. The estimated IAD values for LS Fe are shown in the yellow area. From previous dynamic compression experiments, the Hugoniot of olivine crosses the melting line at ~150 GPa (see fig. S5) (*27*). The light and dark pink areas indicate the onset of melting and the melting regime along the olivine Hugoniot, respectively. The IAD values measured for a statically compressed $(Mg_{0.8}Fe_{0.2})SiO_3$ glass (gPx, black line) are shown for comparison (*14*).

There are no data on Fe partitioning between silicate melt and coexisting solids at pressures above 150 GPa. If the spin state of Fe is the main factor for the Fe partitioning as discussed above, then our data combined with existing studies on spin state of Fe in silicates allow us to make predictions for the pressure range important for larger rocky planets. Existing computational results suggest that $MgSiO_3$ postperovskite would remain stable up to ~600 GPa (*34*), which is expected for the CMB pressure of a ~1.5 $R(E)$ planet. (Mg,Fe)O could maintain a NaCl-like structure with LS Fe or a CsCl-like structure with intermediate spin Fe (intermediate spin) up to that pressure (*35*). As the coordination environment plays a key role in determining the spin state of Fe, the stability of postperovskite may lead to the spin state of Fe in solid phases being mixed spin (i.e., LS Fe in Fp and HS + LS Fe in postperovskite) (*36*).

If LS Fe continues to be more stable in silicate melt at higher pressures, then Fe could continue to partition into silicate melts in the deep interiors of larger super-Earths. However, future investigation of the properties of Fe in silicate melts at greater pressures is needed. Beyond ~1.5 $R(E)$, the peak pressures in the mantle reach more than 600 GPa, where computational studies have predicted the appearance of Mg_2SiO_4 and $MgSi_2O_5$ phases, possibly eliminating Fp from the mineralogy if the mantle composition is Earth-like, Mg/Si >1 (*34*). However, the spin state of Fe in these phases is unknown. Potential mineralogy changes, such as this, raise an intriguing possibility that Fe partitioning and density contrast between silicate melt and solids could be size dependent among rocky planets. This size dependence is clearer for Mars-size smaller rocky planets where Fe in melt likely remains HS for the entire pressure range of the expected magma ocean, and therefore, silicate melt may not have the necessary properties to form a basal magma ocean.

This study demonstrates that combined femtosecond XES and XRD using an XFEL on dynamically compressed planetary materials opens up opportunities to understand atomic-scale processes occurring under extreme pressure-temperature conditions inside the Earth and super-Earth–sized rocky planets. This development is also timely given ongoing and upcoming missions for some of these worlds, such as InSight for Mars, DAVINCI, VERITAS, and EnVision for Venus, and the James Webb Space telescope for exo-rocky planets. Key areas to further advance our knowledge of magma oceans of rocky planets include (i) determining pressure-dependent changes in the Fe spin state of silicate melts at low

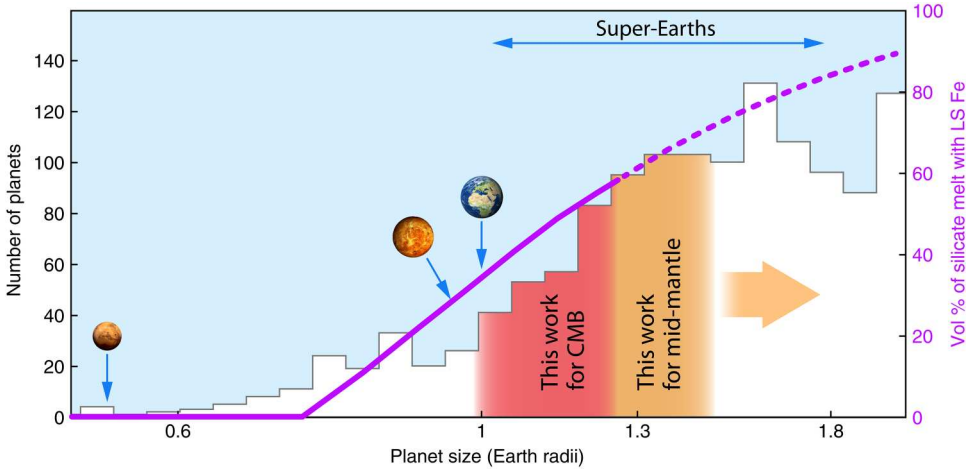

Fig. 4. Implications for a range of rocky planets in the solar system (Mars, Venus, and Earth) and exoplanetary systems. The histogram shows the size distribution of the known exo-planets up to ~1.9 *R*(E). The red area in the histogram highlights the population of the rocky planets with the pressure at the CMB within the pressure range of our experiment. The orange area indicates planets with pressures at the mid-mantle overlapping with our experimental pressure range. If LS Fe continues to be stable to greater pressures than we achieved in this study, then more populations in the super-Earth regime will have deep magma oceans with LS Fe, which is indicated by the orange arrow in the histogram. Assuming 75 GPa for the point where LS Fe begins to dominate in silicate melt (*9*) and Earth-like core mass fraction and mantle composition, we estimate the volume percentage of melt with LS Fe if a rocky planet experienced complete melting of its mantle (purple curve).

pressures, which can further clarify the impact of the Fe spin transition on the density contrast between melt and solid; (ii) determining temperature-dependent changes in the Fe spin state of silicate melts, which can be important for modeling planets with different thermal histories; (iii) direct measurements of melt density during dynamic compression; and (iv) exploring the impact of Fe spin transition on the transport properties of silicate melts, which can be important for the dynamic evolution of basal magma oceans. Such future investigations can provide key information for understanding the diverse evolution paths found in a range of rocky planets in our solar system (Mercury, Mars, Venus, and Earth) and exoplanetary systems.

MATERIALS AND METHODS

Shock target preparation

The starting material was olivine from San Carlos, Arizona. We confirmed the composition of the sample, $(Mg_{0.88}Fe_{0.12})_2SiO_4$, using an electron probe microanalyzer at the Arizona State University. The sample was also examined with Raman spectroscopy for possible inclusions of other minerals. From the screening, we selected pure olivine mineral grains for shock target preparation. The olivine samples were cut into 2 mm–by–2 mm–size platelets and double-sided parallel polished down to thicknesses of 30 to 60 μm, with each sample being individually measured afterward for each target (see the next section for more details). A 50-μm-thick polystyrene or kapton plastic ablator was glued to the optical laser drive side of the sample. The glue layer thickness was measured for each target across the sample at 2.2 ± 1.3 μm. This plastic layer served to smooth out the shock front and improve spatial uniformity during compression. An additional 0.3-μm Al layer was coated on the plastic ablator on the drive side to prevent shine through of the drive laser. The samples were coated with a 2.7-μm Al to enable higher reflectivity for a velocimetry diagnostic, a velocity interferometer system for any reflector (VISAR). An additional Al-coated lithium fluoride (LiF) platelet window (0.15 μm) was glued on some samples to monitor the sample/window interface velocity.

Estimation of thermodynamic state for shock-compressed samples

The thermodynamic state of the shock-compressed olivine samples was retrieved from VISAR interferometry and the known San Carlos olivine Hugoniot (*28*, *37*). We have two approaches for determining pressure: approach 1: for the highest pressure states (above the melting curve), we rely on transit time (i.e., determination of shock breakout in the VISAR and uncertainty in that temporal measurement from the fidelity of the VISAR camera) and the careful metrology of each sample (i.e., we measure the individual thickness of each sample, the glue layer and Kapton, and factor in the uncertainty in this thickness); and approach 2: for lower pressures (below melting), the free surface velocity, U_f, could be measured at the rear side of the target through a fringe shift in the interferometry pattern, with or without impedance mismatch technique applied according to presence of a LiF window. In each case, the uncertainties are determined by SE propagation, which accounts for each variable and SDs. For most of the shots reported in this study, shock pressure is such that the initially (partially) transparent olivine samples are turned opaque or slightly reflective (reflectivity of a few percent, not measurable in our setup). In this configuration, the shock transit time is used to get the mean shock velocity, U_s, knowing the target thickness (fig. S1). For each sample, thickness and planarity have been measured before the experiment using confocal imagery and interferometry with an accuracy of <100 nm. Measurements at different locations of the sample surface have been collected and used for the error estimation. Knowing the target thickness and uncertainty and measuring the breakout time of each shot, we determine U_s. The uncertainty on U_s includes error propagation from the target thickness uncertainty and the breakout time uncertainty. We then applied the previously determined equation of state from (*28*) to calculate the pressure from their U_s -*P*

relationship. The uncertainty in U_s was then used to determine the pressure uncertainty. Here, the U_s error bars could be judged to be relatively large—this has been done in an effort to be conservative with the data and peak pressure, and we used these in the determination of the pressure and pressure uncertainty to capture the maximum pressure uncertainty in the experiment. During the experiment, an x-ray–only shot acquired without the shock drive laser allowed to identify the region probed by the x-ray beam (50 μm) on the VISAR image through a drop in reflectivity of the Al coating. For the real shot, the target was slightly moved to a fresh spot, and the transit time was measured in the correspondence of the x-ray probed region, to avoid eventual effects linked to the shock curvature.

For lower pressures (below melting), the free surface velocity, U_f, could be measured at the target rear side through a fringe shift in the interferometry pattern. Examples of VISAR raw data are shown in fig. S1 for runs #84 and #219 corresponding to pressures of 103 ± 20 GPa and 203 ± 30 GPa, respectively. Using the approximation of $U_f = 2U_p$, valid at moderate pressures, we could directly infer the fluid velocity, U_p. These U_p measurements were approached in two ways: (i) as determined from free surface U_f (where reflectivity in the sample was still maintained, typically at the lower pressures conditions) and (ii) from the sample/LiF interface velocity and applying the impedance mismatch technique to determine the U_p in the sample. In either case, the uncertainty in the U_p was then included in the pressure determination and pressure uncertainty using the previously determined equation of state from (*28*). The thermodynamic state of the shocked sample is then obtained from velocity measurements using existing Hugoniot data (*28*, *37*). Similarly, the fluid velocity (U_p) can be directly inferred in the targets with LiF windows, following the sample/LiF interface velocity and applying the impedance mismatch technique. In the last two cases, a consistency well within the error bars has been found for the thermodynamic state inferred from mean shock velocity and fluid velocity. Here, for each pressure determination approach, we track the uncertainties accordingly: (i) the highest pressures (above melt) depend on shock breakout times and individual thickness measurements of targets and uncertainties in those thicknesses, (ii) U_f at the lower pressure range where there was not a LiF window, and (iii) U_p from impedance matching with sample to LiF. Again, in each case, the uncertainties are determined by SE propagation, which accounts for each variable and SDs, and we have carefully tracked and propagated this through to the pressure values and pressure uncertainties. From the shock velocity and/or the fluid velocity measured from the VISAR, we can infer the density using the known olivine Hugoniot curve. Density values are particularly useful as they are directly related to the Q_1 and the Q_2 peak positions (*24*). We can therefore use the VISAR retrieved densities and the measured positions of Q_1 and Q_2 and compare their trends with the data found in literature. For the comparison being pertinent when including silicates with different initial densities, Q_1 and Q_2 are plotted as a function of compression (fig. S3). This plot shows a very good agreement with the existing data, both from static and dynamic compressions, supporting our density and pressure estimations.

Independent XRD measurements have been used to cross-check the inferred thermodynamic conditions. In our experiment, density estimations could not be directly extracted from XRD patterns because of the amorphous structure and the limited accessible Q range, insufficient for a pair distribution function analysis. We can instead consider the position of the broad scattering contributions, Q_1 and Q_2, which are directly related to the density (*16*, *24*). In fig. S3, we show Q_1 and Q_2 extracted from our diffraction data as a function of the shock compression, ρ/ρ_0, with shocked sample density ρ given by the optical diagnostics coupled to the olivine Hugoniot from (*28*, *37*). In the same plot, we include data from static and dynamic compression experiments on similar silicates ($MgSiO_3$ glass and Mg_2SiO_4 forsterite). Data for $MgSiO_3$ glass are taken from (*16*). Density values for pressures in the static compression experiment are obtained using the equation of state from (*38*). Shock-compressed forsterite data are from (*25*) and using equation of state from (*39*, *40*). We chose to consider compression to account for different initial densities in the various silicates. Our data are well in line with the existing data, supporting our estimations for density and pressure from optical data.

XES and XRD

Kβ XES spectra were measured with the XRD and VISAR at the MEC end-station of the Linac Coherent Light Source (LCLS) simultaneously during the dynamic compression using quasi-monochromatic (0.2 to 0.5% for *dE/E*) x-ray pulses of ~50 fs at 9 keV. The x-rays were focused down to a 50-μm-diameter spot by means of beryllium compound refractive lenses. The x-ray spot size was smaller than the flat compressed region and therefore avoided the detection of pressure and temperature gradients. The XES spectra were collected in a shot-by-shot mode by means of a multicrystal energy-dispersive spectrometer using a von Hamos geometry (*41*). The spectrometer consists of an array of 16 cylindrically bent crystal analyzers (500-mm radius) that diffract and focus the emitted signal onto a position-sensitive detector. The spectrometer is used at Bragg angles close to backscattering to optimize the solid angle per energy and the energy resolution. The angle between the incident and emitted x-rays (scattering angle) is set to 90° to minimize the contribution of the unwanted elastic scattering from the sample (when linearly polarized photons are used). The sample and detector are positioned on the axis of curvature of the crystal analyzers. The vertical position of the crystal array, relative to the sample, defines the Bragg angle and therefore the energy region of interest. The entire array is mounted on a stage with vertical and horizontal travel range of 40 mm, which allows the optimization of the signal and focus on the two-dimensional (2D) detector. The curvature direction of the analyzers provides focusing, whereas the perpendicular direction gives the energy dispersion. For each crystal analyzer, integration along the focusing direction of the signal on the 2D detector results in an emission spectrum.

Considering (i) the x-ray attenuation length for the 9-keV incoming photons used in this study, (ii) the 7.1-keV Fe Kβ XES outcoming photons for the Fe-bearing silicates measured here, and (iii) the geometry of the XES measurement (with the XES outcoming photons reaching the spectrometer at an angle of 60° in the vertical direction from the incoming photons), our calculations show that most of the XES signal is arising from the first 10 μm of the sample. Given the thickness of our samples is in the 40- to 60-μm range, the effect of the x-ray arrival time does not significantly affect the XES spectra as it is purely probing the shocked volume. This calculation was conducted using The Center for X-Ray Optics (CXRO) x-ray interactions with matter databases created by the Lawrence-Berkeley National Laboratory (*42*).

To estimate the spin moment from XES spectra, we calculated the absolute values of the difference spectra (IAD) following the method in (*29*). Our XES spectra measured before shock serve as the HS standard. However, the LS standard is not available for olivine melt. Therefore, we normalized IAD values with respect to 1-bar spectra following the method presented in (*14*). The decrease in satellite peak intensity was observed regardless of the analytical methods used, e.g., IAD method (*29*) or IRD method (*15*). To parameterize these two changes together, we integrated the differences between during- and before-shock spectra and plotted them in Fig. 2. The spectral changes are consistent with a decrease in spin moment (or transition from HS configuration to LS of Fe in silicates and oxides) (*17*, *29*).

XRD patterns were acquired simultaneously with the XES spectra for every x-ray pulse during dynamic compression. The x-ray pulses used to probe the sample are described above in the XES and XRD section. The diffraction images were obtained with Cornell-SLAC Pixel Array Detectors (CSPADs). The detectors were calibrated with LaB_6 for tilting and distance from the sample. The data were processed using the pyFAI package (*43*).

Calculation of LS magma volume fraction in large rocky planets

For Fig. 4, we calculated the mass-radius relations of Earth-like rocky planets using the Burnman code (*44*). In the calculation, we fixed the mantle-to-core mass ratio to that of the Earth. The mass-radius relations are calculated using a two-layer model where the bridgmanite equation of state is used for calculating the mantle and the Fe metal equation of state is used for calculating the core. It is well known that calculations based on such assumptions can still reproduce Earth's radius and mass well enough for the exoplanet data analysis. From the mass-radius relation, we then calculate pressure profiles of super-Earths with different mass (and radius). Difference in temperature profiles of the super-Earths is not considered here because the temperature profile would likely vary a lot because of various factors including differences in the inventories of heat producing elements. However, we note that the temperature variation for the spin population is likely small compared with the pressure range of the super-Earths: approximately a 30-GPa change in spin transition pressure over a 3000-K temperature change (*8*).

Supplementary Materials

This PDF file includes:

Figs. S1 to S5
Table S1
References

REFERENCES AND NOTES

1. W. B. Tonks, H. J. Melosh, Magma ocean formation due to giant impacts. *J. Geophys. Res. Planets* **98**, 5319–5333 (1993).
2. S. Labrosse, J. Hernlund, N. Coltice, A crystallizing dense magma ocean at the base of the Earth's mantle. *Nature* **450**, 866–869 (2007).
3. M. D. Ballmer, D. L. Lourenço, K. Hirose, R. Caracas, R. Nomura, Reconciling magma-ocean crystallization models with the present-day structure of the Earth's mantle. *Geochem. Geophys. Geosyst.* **18**, 2785–2806 (2017).
4. E. J. Garnero, A. K. McNamara, S.-H. Shim, Continent-sized anomalous zones with low seismic velocity at the base of Earth's mantle. *Nat. Geosci.* **9**, 481–489 (2016).
5. R. Caracas, K. Hirose, R. Nomura, M. D. Ballmer, Melt–crystal density crossover in a deep magma ocean. *Earth Planet. Sci. Lett.* **516**, 202–211 (2019).
6. N. A. Blanc, D. R. Stegman, L. B. Ziegler, Thermal and magnetic evolution of a crystallizing basal magma ocean in Earth's mantle. *Earth Planet. Sci. Lett.* **534**, 116085 (2020).
7. E. Stolper, D. Walker, B. H. Hager, J. F. Hays, Melt segregation from partially molten source regions: The importance of melt density and source region size. *J. Geophys. Res. Solid Earth* **86**, 6261–6271 (1981).
8. B. B. Karki, D. B. Ghosh, C. Maharjan, S.-I. Karato, J. Park, Density-pressure profiles of fe-bearing $MgSiO_3$ liquid: Effects of valence and spin states, and implications for the chemical evolution of the lower mantle. *Geophys. Res. Lett.* **45**, 3959–3966 (2018).
9. R. Nomura, H. Ozawa, S. Tateno, K. Hirose, J. Hernlund, S. Muto, H. Ishii, N. Hiraoka, Spin crossover and iron-rich silicate melt in the Earth's deep mantle. *Nature* **473**, 199–202 (2011).
10. T. Kim, B. Ko, E. Greenberg, V. Prakapenka, S.-H. Shim, Y. Lee, Low melting temperature of anhydrous mantle materials at the core-mantle boundary. *Geophys. Res. Lett.* **47**, e2020GL089345 (2020).
11. Y. Fei, L. Zhang, A. Corgne, H. Watson, A. Ricolleau, Y. Meng, V. Prakapenka, Spin transition and equations of state of (Mg, Fe)O solid solutions. *Geophys. Res. Lett.* **34**, L17347 (2007).
12. J. Braithwaite, L. Stixrude, Partitioning of iron between liquid and crystalline phases of (Mg, Fe)O. *Geophys. Res. Lett.* **49**, e2022GL099116 (2022).
13. L. Stixrude, R. Scipioni, M. P. Desjarlais, A silicate dynamo in the early earth. *Nat. Commun.* **11**, 935 (2020).
14. C. Gu, K. Catalli, B. Grocholski, L. Gao, E. Alp, P. Chow, Y. Xiao, H. Cynn, W. J. Evans, S.-H. Shim, Electronic structure of iron in magnesium silicate glasses at high pressure. *Geophys. Res. Lett.* **39**, L24304 (2012).
15. Z. Mao, J.-F. Lin, J. Yang, J. Wu, H. C. Watson, Y. Xiao, P. Chow, J. Zhao, Spin and valence states of iron in Al-bearing silicate glass at high pressures studied by synchrotron Mossbauer and x-ray emission spectroscopy. *Am. Mineral.* **99**, 415–423 (2014).
16. G. Morard, J.-A. Hernandez, M. Guarguaglini, R. Bolis, A. Benuzzi-Mounaix, T. Vinci, G. Fiquet, M. A. Baron, S. H. Shim, B. Ko, A. E. Gleason, W. L. Mao, R. Alonso-Mori, H. J. Lee, B. Nagler, E. Galtier, D. Sokaras, S. H. Glenzer, D. Andrault, G. Garbarino, M. Mezouar, A. K. Schuster, A. Ravasio, In situ x-ray diffraction of silicate liquids and glasses under dynamic and static compression to megabar pressures. *Proc. Natl. Acad. Sci. U.S.A.* **117**, 11981–11986 (2020).
17. J. Badro, Spin transitions in mantle minerals. *Annu. Rev. Earth Planet. Sci.* **42**, 231–248 (2014).
18. E. Holmström, L. Stixrude, Spin crossover in liquid (Mg, Fe)O at extreme conditions. *Phys. Rev. B* **93**, 195142 (2016).
19. I. Leonov, Metal-insulator transition and local-moment collapse in FeO under pressure. *Phys. Rev. B* **92**, 085142 (2015).
20. S. Tateno, K. Hirose, Y. Ohishi, Melting experiments on peridotite to lowermost mantle conditions. *J. Geophys. Res. Solid Earth* **119**, 4684–4694 (2014).
21. C. Prescher, C. Weigel, C. McCammon, O. Narygina, V. Potapkin, I. Kupenko, R. Sinmyo, A. Chumakov, L. Dubrovinsky, Iron spin state in silicate glass at high pressure: Implications for melts in the Earth's lower mantle. *Earth Planet. Sci. Lett.* **385**, 130–136 (2014).
22. R. Sinmyo, K. Hirose, The soret diffusion in laser-heated diamond-anvil cell. *Phys. Earth Planet. In.* **180**, 172–178 (2010).
23. P. Emma, R. Akre, J. Arthur, R. Bionta, C. Bostedt, J. Bozek, A. Brachmann, P. Bucksbaum, R. Coffee, F.-J. Decker, Y. Ding, D. Dowell, S. Edstrom, A. Fisher, J. Frisch, S. Gilevich, J. Hastings, G. Hays, P. Hering, Z. Huang, R. Iverson, H. Loos, M. Messerschmidt, A. Miahnahri, S. Moeller, H. D. Nuhn, G. Pile, D. Ratner, J. Rzepiela, D. Schultz, T. Smith, P. Stefan, H. Tompkins, J. Turner, J. Welch, W. White, J. Wu, G. Yocky, J. Galayda, First lasing and operation of an ångstrom-wavelength free-electron laser. *Nat. Photonics* **4**, 641–647 (2010).
24. J.-A. Hernandez, G. Morard, M. Guarguaglini, R. Alonso-Mori, A. Benuzzi-Mounaix, R. Bolis, G. Fiquet, E. Galtier, A. E. Gleason, S. Glenzer, F. Guyot, B. Ko, H. J. Lee, W. L. Mao, B. Nagler, N. Ozaki, A. K. Schuster, S. H. Shim, T. Vinci, A. Ravasio, Direct observation of shock-induced disordering of enstatite below the melting temperature. *Geophys. Res. Lett.* **47**, e2020GL088887 (2020).
25. D. Kim, S. J. Tracy, R. F. Smith, A. E. Gleason, C. A. Bolme, V. B. Prakapenka, K. Appel, S. Speziale, J. K. Wicks, E. J. Berryman, S. K. Han, M. O. Schoelmerich, H. J. Lee, B. Nagler, E. F. Cunningham, M. C. Akin, P. D. Asimow, J. H. Eggert, T. S. Duffy, Femtosecond x-ray diffraction of laser-shocked forsterite (Mg_2SiO_4) to 122 GPa. *J. Geophys. Res. Solid Earth* **126**, e2020JB020337 (2021).
26. C. Prescher, V. B. Prakapenka, J. Stefanski, S. Jahn, L. B. Skinner, Y. Wang, Beyond sixfold coordinated Si in SiO_2 glass at ultrahigh pressures. *Proc. Natl. Acad. Sci. U.S.A.* **114**, 10041–10046 (2017).
27. S.-N. Luo, J. A. Akins, T. J. Ahrens, P. D. Asimow, Shock-compressed $MgSiO_3$ glass, enstatite, olivine, and quartz: Optical emission, temperatures, and melting. *J. Geophys. Res. Solid Earth* **109**, B05205 (2004).

28. B. Chidester, M. Millot, J. Townsend, D. Spaulding, E. Davies, S. Root, P. Kalita, D. Fratanduono, S. Jacobsen, S. Stewart, The principal hugoniot of iron-bearing olivine to 1465 GPa. *Geophys. Res. Lett.* **48**, e2021GL092471 (2021).
29. G. Vankó, T. Neisius, G. Molnar, F. Renz, S. Karpati, A. Shukla, F. M. De Groot, Probing the 3*d* spin momentum with x-ray emission spectroscopy: The case of molecular-spin transitions. *J. Phys. Chem. B.* **110**, 11647–11653 (2006).
30. G. Fiquet, A. Auzende, J. Siebert, A. Corgne, H. Bureau, H. Ozawa, G. Garbarino, Melting of peridotite to 140 gigapascals. *Science* **329**, 1516–1518 (2010).
31. D. Andrault, S. Petitgirard, G. L. Nigro, J.-L. Devidal, G. Veronesi, G. Garbarino, M. Mezouar, Solid–liquid iron partitioning in Earth's deep mantle. *Nature* **487**, 354–357 (2012).
32. F. Soubiran, B. Militzer, Electrical conductivity and magnetic dynamos in magma oceans of super-Earths. *Nat. Commun.* **9**, 3883 (2018).
33. J. G. O'Rourke, Venus: A thick basal magma ocean may exist today. *Geophys. Res. Lett.* **47**, e2019GL086126 (2020).
34. K. Umemoto, R. M. Wentzcovitch, S. Wu, M. Ji, C.-Z. Wang, K.-M. Ho, Phase transitions in $MgSiO_3$ post-perovskite in super-Earth mantles. *Earth Planet Sci. Lett.* **478**, 40–45 (2017).
35. H. Hsu, K. Umemoto, Structural transition and re-emergence of iron's total electron spin in (Mg, Fe)O at ultrahigh pressure. *Nat. Commun.* **13**, 2780 (2022).
36. H. Hsu, G. Y. Yonggang, R. M. Wentzcovitch, Spin crossover of iron in aluminous $MgSiO_3$ perovskite and post-perovskite. *Earth Planet Sci. lett.* **359**, 34–39 (2012).
37. J. M. Brown, M. D. Furnish, R. G. Mcqueen, Thermodynamics for $(Mg,Fe)_2SiO_4$ from the Hugoniot, in *High-Pressure Research in Mineral Physics: A Volume in Honor of Syun-iti Akimoto*, M. H. Manghnani, Y. Syono, Eds. (American Geophysical Union, 1987), pp. 373–384.
38. S. Petitgirard, W. J. Malfait, R. Sinmyo, I. Kupenko, L. Hennet, D. Harries, T. Dane, M. Burghammer, D. C. Rubie, Fate of $MgSiO_3$ melts at core–mantle boundary conditions. *Proc. Natl. Acad. Sci.U.S.A.* **112**, 14186–14190 (2015).
39. J. L. Mosenfelder, P. D. Asimow, T. J. Ahrens, Thermodynamic properties of Mg_2SiO_4 liquid at ultra-high pressures from shock measurements to 200 GPa on forsterite and wadsleyite. *J. Geophys. Res. Solid Earth* **112**, B06208 (2007).
40. S. Root, J. P. Townsend, E. Davies, R. W. Lemke, D. E. Bliss, D. E. Fratanduono, R. G. Kraus, M. Millot, D. K. Spaulding, L. Shulenburger, S. T. Stewart, S. B. Jacobsen, The principal hugoniot of forsterite to 950 GPa. *Geophys. Res. Lett.* **45**, 3865–3872 (2018).
41. R. Alonso-Mori, J. Kern, D. Sokaras, T.-C. Weng, D. Nordlund, P. Tran, R. A. Mon-tanez, J. Delor, V. K. Yachandra, J. Yano, U. Bergmann, A multi-crystal wavelength dispersive x-ray spectrometer. *Rev. Sci. Instrum.* **83**, 073114 (2012).
42. B. L. Henke, E. M. Gullikson, J. C. Davis, X-ray interactions: Photoabsorption, scattering, transmission, and reflection at E = 50-30,000 ev, Z = 1-92. *At. Data. Nucl. Data Tables* **54**, 181–342 (1993).
43. G. Ashiotis, A. Deschildre, Z. Nawaz, J. P. Wright, D. Karkoulis, F. E. Picca, J. Kieffer, The fast azimuthal integration Python library: pyFAI. *J. Appl. Cryst.* **48**, 510–519 (2015).
44. S. Cottaar, T. Heister, I. Rose, C. Unterborn, BurnMan: A lower mantle mineral physics toolkit. *Geochem. Geophys. Geosyst.* **15**, 1164–1179 (2014).
45. R. Alonso-Mori, J. Kern, R. J. Gildea, D. Sokaras, T.-C. Weng, B. Lassalle-Kaiser, R. Tran, J. Hattne, H. Laksmono, J. Hellmich, C. Glöckner, N. Echols, R. G. Sierra, D. W. Schafer, J. Sellberg, C. Kenney, R. Herbst, J. Pines, P. Hart, S. Herrmann, R. W. Grosse-Kunstleve, M. J. Latimer, A. R. Fry, M. M. Messerschmidt, A. Miahnahri, M. M. Seibert, P. H. Zwart, W. E. White, P. D. Adams, M. J. Bogan, S. Boutet, G. J. Williams, A. Zouni, J. Messinger, P. Glatzel, N. K. Sauter, V. K. Yachandra, J. Yano, U. Bergmann, Energy-dispersive x-ray emission spectroscopy using an x-ray free-electron laser in a shot-by-shot mode. *Proc. Natl. Acad. Sci. U.S.A.* **109**, 19103–19107 (2012).
46. C. Benmore, E. Soignard, M. Guthrie, S. Amin, J. Weber, K. McKiernan, M. Wilding, J. Yarger, High pressure x-ray diffraction measurements on Mg_2SiO_4 glass. *J. Non Cryst. Solids* **357**, 2632–2636 (2011).
47. C. Meade, R. J. Hemley, H. Mao, High-pressure x-ray diffraction of SiO_2 glass. *Phys. Rev. Lett.* **69**, 1387–1390 (1992).
48. G. A. Lyzenga, T. J. Ahrens, Shock temperature measurements in Mg_2SiO_4 and SiO_2 at high pressures. *Geophys. Res. Lett.* **7**, 141–144 (1980).

Acknowledgments

Funding: S.-H.S. and B.K. were supported by NSF-EAR-1725094. G.M. and G.F. acknowledge funding from the European Research Council (ERC) under the European Union's Horizon 2020 Research and Innovation program (ERC PlanetDive, grant agreement 670787). A.G. acknowledges the Los Alamos National Laboratory (LANL) Reines Laboratory Directed Research and Development (LDRD). A.G. and W.M. acknowledge support from the NSF Geophysics Program (grant EAR0738873). S.-H.S., A.G., and W.M. acknowledge support from the NSF CSEDI Program (grant EAR2153968) and NASA Exoplanet Program (80NSSC23K0265). R.A.-M was supported by NIH grant 1P41GM139687. This research was also supported by the POMPEI program of the Agence National de la Recherche (grant ANR-16-CE31-0008). Dynamic compression experiments were performed at the MEC instrument of LCLS, supported by the US Department of Energy (DOE) Office of Science, Fusion Energy Science under contract SF00515, FWP 100182, and were supported by LCLS, a National User Facility operated by Stanford University on behalf of the U.S. DOE, Office of Basic Energy Sciences. **Author contributions:** S.-H.S., W.M., G.M., A.R., A.G., and R.A.-M. conceptualized and supervised the project, acquired funding, designed and performed experiments, analyzed data, and wrote the manuscript. B.K. performed the experiments and analyzed data. D.S., B.N., H.L., E.Gr., S.G., and E.Ga. provided resources for the x-ray measurements and supervised the experiments. T.V. and G.F. acquired funding and design the experiments. J.D., J.T., and B.K. prepared the samples. All authors reviewed the manuscript. **Competing interests:** The authors declare that they have no competing interests. **Data and materials availability:** All data needed to evaluate the conclusions in the paper are present in the paper and/or the Supplementary Materials. The data that support the findings of this study are available in Zenodo with the identifier, 10.5281/zenodo.7114910.

Submitted 7 May 2023
Accepted 20 September 2023
Published 20 October 2023
10.1126/sciadv.adi6153

ScienceAdvances

Ultrafast x-ray detection of low-spin iron in molten silicate under deep planetary interior conditions

Sang-Heon Shim, Byeongkwan Ko, Dimosthenis Sokaras, Bob Nagler, He Ja Lee, Eric Galtier, Siegfried Glenzer, Eduardo Granados, Tommaso Vinci, Guillaume Fiquet, Jonathan Dolinschi, Jackie Tappan, Britany Kulka, Wendy L. Mao, Guillaume Morard, Alessandra Ravasio, Arianna Gleason, and Roberto Alonso-Mori

Sci. Adv. **9** (42), eadi6153. DOI: 10.1126/sciadv.adi6153

Science Advances (ISSN 2375-2548) is published by the American Association for the Advancement of Science. 1200 New York Avenue NW, Washington, DC 20005. The title *Science Advances* is a registered trademark of AAAS.